

Article citation info:

Ferdynus M, Gajewski J. Identification of crashworthiness indicators of column energy absorbers with triggers in the form of cylindrical embossing on the lateral edges using artificial neural networks. *Eksploracja i Niezawodność – Maintenance and Reliability* 2022; 24 (4): 805–821, <http://doi.org/10.17531/ein.2022.4.20>

Identification of crashworthiness indicators of column energy absorbers with triggers in the form of cylindrical embossing on the lateral edges using artificial neural networks

Indexed by:



Mirosław Ferdynus^{a,*}, Jakub Gajewski^a

Lublin University of Technology, Department of Machine Construction & Mechatronics, Lublin, Poland

Highlights

- The possibility of using artificial neural networks to identify the most advantageous variants of column energy is shown
- The considered design variants differ in geometric parameters and the position of the trigger
- The research was carried out with the use of FEM, and the models were validated by the experiment
- It has been shown that the use of neural networks to predict the properties of the energy absorber is possible with a slight error in relation to the time-consuming multi-variant FEM analyzes.

Abstract

The paper presents the possibility of neural network application in order to identify the most advantageous design variants of column energy absorbers in terms of the achieved energy absorption indicators. Design variants of the column energy absorber made of standard thin-walled square aluminium profile with triggers in the form of four identical cylindrical embossments on the lateral edges were considered. These variants differ in the diameter of the trigger, its depth and position. The geometrical parameters of the trigger are crucial for the energy absorption performance of the energy absorber. The following indicators are studied: PCF (Peak Crushing Force), MCF (Mean Crushing Force), CLE (Crash Load Efficiency), SE (Stroke Efficiency) and TE (Total Efficiency). On the basis of numerical studies validated by experimentation, a neural network has been created with the aim of predicting the above-mentioned indices with an acceptable error for an energy absorber with the trigger of specified geometrical parameters and position. The paper demonstrates that the use of an effective multilayer perceptron can successfully speed up the design process, saving time on multivariate time-consuming analyses.

Keywords

crashworthiness indicators, energy absorber, thin-walled tube, artificial neural network.

This is an open access article under the CC BY license (<https://creativecommons.org/licenses/by/4.0/>)

List of abbreviations used in the article

ANN- Artificial Neural Network,
CFE- Crash Force Efficiency,
CFRP- Carbon Fiber Reinforced Polymer,
CLE- Crash Load Efficiency,
EA- Energy Absorbed,
FE- Finite Element,
FE- Finite Element Method,
FMST- Foam-filled Multi-cell Thin-walled Structures,
GA- Genetic Algorithm,
MCF- Mean Crushing Force,
MOD- Multi-objective Optimization Design,
PCF- Peak Crushing Force,
RP- Reference Point,
SEA- Specific Energy Absorbed,
SE- Stroke Efficiency,
TE- Total Efficiency,

TOPSIS- Technique for Ordering Preferences by Similarity to ideal Solution,
TW- Thin-Walled,

1. Introduction, motivation and objectives of the research

In the times of increasingly intensive traffic on the roads and higher speeds reached by vehicles, the passive safety of motor vehicles is becoming a very important issue often determining the survival of the traveling people. One of the key aspects of passive safety is a properly designed crumple zone, of which crash boxes are a very important element. Crash boxes are mounted on the side members inside the engine compartment, connected by a rigid beam, which is hidden under the bumper and is designed to absorb energy in low-speed crashes (15-20 km/h) protecting the above-mentioned side members from damage, which is costly and time-consuming to repair. This makes a big difference to vehicle operation in terms of repair costs and time out of service. The presence of crash boxes at higher speeds is also

(*) Corresponding author.

E-mail addresses: M. Ferdynus (ORCID: 0000-0003-0348-631X): m.ferdynus@pollub.pl, J. Gajewski (ORCID: 0000-0001-8166-7162): j.gajewski@pollub.pl

important, as they are able to absorb quite a large portion of energy for their size, which consequently leads to much less destruction of this part of the vehicle and in the case of extremely high energies increases the chances of survival of the driver and passengers.

In the modern design process, the artificial neural network technique is often used among other things because of its high predictive capability, which makes it possible to arrive at optimal solutions at a lower cost. Simplifying, a typical ANN acts like a black box, transforming input data into output data by applying various learning procedures. An ANN mimics biological neurons in that it has many non-linear computational agents working in parallel. All these computational agents are tightly coupled by weights, which are carefully modified by learning algorithms to improve their prediction performance or to search for optimal, maximum or minimum values. In this paper, ANN is used to predict the values of energy-absorption indicators in relation to the geometrical parameters of the trigger and its position.

The main objective of this study is to present the possibility of using a neural network to identify the most favourable design variants of column energy absorbers in terms of the energy absorption rates achieved. Design variants of the energy absorber in the form of a thin-walled square column made of aluminium alloy with triggers in the form of four identical cylindrical embossments on the lateral edges were considered. The variants differ in the diameter of the trigger, its depth and position. The geometrical parameters of the trigger are crucial to the energy absorption performance of the absorber. The main task of the work was therefore, based on numerical studies verified experimentally, to create a neural network that would predict energy-absorption rates with acceptable error for an energy absorber with a trigger with specific geometrical parameters and position.

2. State of art: an overview

Designers of crumple zones intended to absorb impact energy must satisfy two major, often conflicting requirements: minimizing the initial load while maximizing the amount of energy absorbed. The initial load at the moment of impact must not be too high to avoid excessive decelerations during vehicle impact (biomechanical reasons). On the other hand, the main requirement is the maximum possible energy absorption and dissipation capacity to make these zones effective. Therefore, it is important, the search for an optimal design of these elements, maximize the energy absorption and minimize the ratio of the initiating peak crushing force (PCF) to the mean crushing force (MCF).

Thin-walled metal tubes, are broadly used as energy absorbers because they are relatively cheap and efficient in absorbing energy. Square, rectangular or circular tubes are commonly used but other cross-section shapes have also been analyzed for their suitability [7, 31], as well as multi-cornered [1, 35] multi-cell [12, 28, 42] and bi-tubal designs [38, 45]. The behavior of these types of structures during axial, oblique and lateral crushing has been extensively studied over the past decades. This research has been reflected in numerous publications, among which review articles have been published more and more over the years [6, 9, 40, 43]. Abramowicz [2] presented deep considerations based on analytical description and experimental studies of thin-walled structures subjected to axial crushing force, although the first paper appeared much earlier in the 1960s [5]. However, mainly due to the underdevelopment of numerical methods, it took another decades before the field could develop. Many relevant papers were presented in the 1st International Symposium on Structural Crashworthiness held in Liverpool in 1983, which were collected in a special issue of the International Journal of Mechanical Science (9/10, 1983). At that time, valuable books also appeared [49–51].

In his work [6] Alghamdi was one of the first to systematize the works that appeared until the end of the 20th century, dividing energy absorbers according to the shape of the cross-section but also the way of operation. Nurick et al [43], on the other hand, limited their

review to axially impacted tubular structures to which imperfections in the form of recesses, notches or combinations thereof were introduced, but also presented interesting results for “prebuckle” structures. Hollow or foam-filled structures were considered. A separate section describes the behavior of structures that are ripped into strips during axial impact. On the other hand, publication [9] based on an extensive literature review, presents a comprehensive review of recent developments in the crashworthiness of TW tubes used in vehicles, with a focus on topics that have emerged in the last fifteen years, such as crash optimization design and energy absorption responses of unconventional thin-walled components, including multi-cell tubes, functionally graded thickness tubes. Both hollow and foam-filled structures operating under axial, lateral, oblique, and bending loads were considered, including foam-filled structures with graded functionality. The paper [40] mainly discusses the current state of knowledge on energy absorption of gradient structures and materials and the effect of gradient properties on their crashworthiness. These advanced energy-absorbing structures and materials primarily include thin-walled structures with variable diameter/width/wall thickness/strength, variable density cellular materials and their filler structures, and other hybrid structures with multiple graded properties. It is undoubtedly a very developing direction, pursued both by academia and industry. An example of a publication where crashworthiness issues are presented in various aspects of aero-structure design and testing is work of Xianfeng Yang et al. [41] presenting a systematic review of the literature and specific helicopter design solutions. Also noteworthy are the very valuable, even fundamental books [19, 27] on which crashworthiness researchers are based, as evidenced by the fact how often they are quoted.

In the work of Langseth et al [24], extrusions with square cross-section, made of aluminum alloy, were subjected to static and dynamic analysis. Both experimental studies and numerical simulations (LS-DYNA code) were carried out. The specimens were prepared with a small trigger in the form of embossments on opposite walls. Tests were conducted for two variants of its position: in the middle plane and on top. The behavior of the structure was tested at different tup weights and different impact velocities. Both the initiating peak crushing force PCF and the mean crushing force MCF were calculated.

In publication [4], Alavi Nia et al conducts a study of aluminum thin-walled structures with triangular, square, hexagonal and octagonal cross-section made in two multi-cell and one hollow variants. It has been shown that regardless of the configuration of the location of the inner walls of multi-cells, the SEA (Specific Energy Absorbed) is always greater than for the profile in a simple form, while the variant in which the inner walls of multi-cells connect with the outer profile in the middle of the walls and not at the corners is much more advantageous. Another very important conclusion that disqualifies multi-cell profiles from certain applications is that there is a 30 to 120% increase in PCF force compared to a plain profile, and this result is obtained for quasi-static tests and can be even higher for dynamic tests. Such an increase will result in a drastic increase in overload during the initial crush phase. Unfortunately, CLE values are not under investigation and it is uncertain whether the CLE value (Crash Load Efficiency) ultimately decreased or increased despite the increase in PCF and MCF.

The paper [25] analyzed the effect of the placement of triggers in the form of grooves on square section profiles on the PCF (called maximum compressive repulsive force by the authors) and the amount of energy absorbed. The optimal groove layout was obtained by introducing indentations with a pitch corresponding to the fold wavelength accurately estimated from the computer simulation. An important conclusion is that excessive concentration of triggers although leads to a reduction in PCF the member undergoes destruction which is a combination of global buckling and progressive folding and as a result does not absorb energy as well. Incidentally, this is one of the first papers, and unfortunately few, in which the triggering mechanism was properly appreciated. In many papers the role of triggers is down-

played as if their role was limited only to the initiation of the crushing process, while their influence on the achieved parameters, especially CLE, is undeniable.

In a paper published by Rai et al [34], two decades later, the effect of the triggering mechanism on the crushing force efficiency of aluminum tubular absorbers was investigated. Different triggering mechanisms such as cut-out, circumferential notch and end-fillet were investigated using a validated numerical model. Based on the numerical and experimental results, it was found that tubes made of aluminum showed better crashworthiness compared to steel tubes. According to these results, the developed trigger mechanisms significantly change the crash performance of tubular absorbers. The crushing force efficiency doubled with the most effective trigger mechanism, while the stroke and specific energy absorption efficiencies decreased by 4% and 15%, respectively.

Very interesting results concerning the triggering mechanism and circumferential stresses in thin-walled tubes of square and circular cross-sections, whose geometry was perturbed by the use of corrugations are presented in [11]. Undoubtedly, this work should be continued as far as the determination of energy absorption coefficients is concerned. On the other hand, in the work of Zhang et al. [46] numerical investigations were presented concerning the course of the crushing process and the improvement of energy absorption achieved by applying pyramidal embossments arranged in a certain pattern on the whole lateral surface of the specimen in two configurations but also with different number of pyramids placed on the specimen depending on the size of a single base element. Also this valuable work demands, after overcoming technological problems, experimental verification.

A very valuable publication is the work of Karagiozova and Jones [20] where the dynamic elastic-plastic buckling of thin-walled square tubes was studied from the point of view of the propagation of the elastic-plastic stress wave that originated from axial impact load. The influence of the impact velocity and the striking mass on the development of the buckling shape was discussed when considering the transient deformation process. The wave behavior in square tubes was also compared with geometrically equivalent circular tubes.

Axial crushing of square crash boxes was also the subject of a very interesting publication by Jafarzadeh-Aghdam and Schröder [18], where the authors addressed the problems of experimental validation and the large number of irreproducible test results. There is an interesting description of the influence of stress wave propagation, existing imperfections as a source of this irreproducibility.

At the turn of the centuries, a new class of tubular energy absorbers emerged, which are classic axially loaded thin-walled metal columns filled with foam or honeycomb structures. Energy absorbers of this type absorb energy during the crushing process both through phenomena in the metal profile itself and in the filling. Due to the existence of many parameters affecting the energy absorption capacity of such columns and the interaction between the outer shell and the filling, optimization procedures had to be developed. One of the first attempts in this field was published by Zarei and Kroger [44], who performed an optimization of a tube filled with aluminum foam and also analyzed hollow tubes.

In the first decade of the 21st century, multi-cell columns, both empty and filled with foam, were implemented as energy absorbers [12]. Yin et al [42] presented the results obtained using the non-linear LS-DYNA finite element code, for six types of foam-filled multi-cell thin-walled structures (FMTS) with different cell numbers. During the process of multi-objective optimization design (MOD), four kinds of commonly used metamodels was established to reduce the computational cost of crash simulations by the finite element method. A very interesting concept of energy absorbing structure was presented in Luo's work [28], where the energy absorption properties of square tubes have been significantly increased by replacing ultra-thin solid walls into sandwich walls. On the other hand, W. Liu et al. in paper [26], performed multi-objective crash optimization of star sandwich tubes. A rather promising approach to improve the energy efficiency

and impact performance of thin-walled structures was proposed by Zhang et al in their paper [48], by introducing a thickness gradient in the cross-section. Experimental studies were first carried out for square tubes with two types of thickness distribution, and only then FE numerical analyses were carried out to confirm the experimental results. On the other hand, in the paper [33], the authors addressed the issue of evaluating the crashworthiness of newly designed multicellular structures with different structural forms (i.e. square, hexagonal, octagonal, decagonal and circular). The optimisation problem consisted of minimising the PCF and maximising the SEA and the variables were geometrical parameters related to the cross-sectional area and, more specifically, to the ratio of the inner and outer tube dimensions. Geometrical dimensions of these structures were optimized using ANNs and GA (genetic algorithm) by considering three different scenarios. The optimal structures were compared together from the crashworthiness point of view by considering two conflicting crashworthiness indicators namely SEA and PCF using a decision making method called TOPSIS (technique for ordering preferences by similarity to ideal solution).

The paper [16] presents the results of numerical tests of impact and energy absorption capacity of thin-walled aluminum columns, having a square cross-section and spherical indentations on their lateral surfaces. The numerical models were validated using an experiment conducted on the drop hammer. The crushing behavior of the columns and some crashworthiness indicators were investigated. The most beneficial design/construction alternatives in terms of achieved crash performance have been indicated. Numerical analysis of the thin-walled structure with different trigger locations was also conducted in article [36].

The article by Zhang & Huh [47] presents a numerical study of the behaviour of longitudinally grooved square tubes made of steel during dynamic axial compression. The simulations took into account phenomena such as the distribution of effective plastic strain and thickness changes resulting from the stamping process. Apart from force-displacement characteristics, only PCF and SEA were determined.

The influence of triggers in the form of cylindrical symmetrical indentations located at the edges of columns on the performance of the structure and energy-absorption indicators was analysed in a paper [15], where advanced numerical studies with experimental validation were demonstrated. The present work is a continuation of those considerations.

Optimisation of structural crashworthiness and energy absorption has become an important research topic due to its proven benefits for public safety. Fang et al provide a comprehensive review of the important studies on design optimization for structural crashworthiness and energy absorption [13]. The design criteria used in crashworthiness and energy absorption studies are reviewed and surrogate modelling for evaluating these criteria is discussed. Multi-objective optimization, optimization under uncertainties and topological optimization from concepts, algorithms to applications in crashworthiness studies are also reviewed.

The analysis of bibliography indicates a recent publication on the application of artificial intelligence methods with energy-absorption analysis. Baykasoğlu et al [10] described designs of novel lattice structure filled square thin-walled tubes by using a compromise programming based multi-objective crashworthiness optimization procedure. An artificial neural network is employed for predicting values of the objective functions. Laban et al [23] provides insights into the sensitivity of braided carbon-kevlar round tubes to external damages and neural network-based models that can predict the consequences of damages on the crush behaviour. Paygozar and Dizaji analyzed a damper of high-rise structures using artificial neural network [32]. Literature studies have also shown interesting publications on the use of neural networks and FEM for crashworthiness studies. In a paper [29], Marzbanrad and Elbrahimi conducted a numerical crushing study of thin-walled circular aluminium tubes to investigate their behaviour under axial impact loading for five crushing parameters using multi-

objective optimisation with a weighted sum method. To improve the accuracy of the optimisation process, artificial neural networks were used. A genetic algorithm was also implemented. Finite element code, capable of evaluating the crushing parameters, from which the output is used to train and test the developed neural networks. In Mirzaei et al article [30] the multi-objective optimization of cylindrical aluminium tubes under axial impact load was presented. A back-propagation neural network was constructed as the model to formulate the mapping between variables and objectives. The finite element software ABAQUS/Explicit was used to generate the training database for the network, as in our research. Validating the results of finite element model, several impact tests are carried out using drop hammer. In [37] the finite element model of the CFRP tube was developed using the Tsai-Wu failure criterion to model the crush characteristics. A series of FEM simulations were conducted considering different fiber directions and the number of layers to generate enough data for constructing the artificial neural network.

The literature analysis has shown that more and more research interest is directed towards coupling numerical simulations validated by experiment and analysis using neural networks. There are few works that would give answers to questions concerning the optimal configuration of geometrical parameters of triggers and their location from the point of view of crashworthiness. It was the authors' ambition to at least partially fill this gap. Due to the fact that the triggering mechanism is most effective in simple structures, the consideration was limited to square section structures, which despite the emergence of research on multicell, multicorner and bitubal structures are still widely used due to their simplicity and cheapness. Not without significance is the fact that geometrically more complex structures, despite showing a much higher SEA value compared to simple ones, generate a much higher PCF value which affects the overloads to which the protected object is subjected. This eliminates this type of structures from certain applications.

In this paper [21], the crashworthiness of composite rectangular tubes was analysed using experimental and ANN techniques. Based on the experimentally obtained values of different impact strength parameters under different loading conditions, ANN models were constructed to determine the optimum cross-sectional ratio of the laminated composite to achieve the target mechanical properties, such as load carrying capacity and energy absorption. There are many publications in which artificial intelligence has been used to predict specific parameters. In paper [8] the authors illustrated this using fatigue crack length as an example, while paper [3] applied the network to aircraft engine failure prediction. An interesting look at energy efficiency issues on another technical facility is shown in publication [22].

The literature review shows that the issue of predicting the values of energy-absorbing indices using ANNs is novel and can significantly speed up the process of developing an energy-absorber with the desired parameters. The considerations carried out in this work are of universal character, however, they were conducted on the basis of one type of trigger - a cylindrical symmetrical embossment on the side edge. The influence of geometrical parameters of triggers (diameter of cylindrical embossment and its depth) and their location on the achieved energy absorption indicators was studied. The neural networks created on the basis of validated numerical tests allowed predicting what results in terms of energy absorption rates will be achieved by an energy absorber with a trigger of any set of geometrical parameters and its position. This makes it possible to obtain the result much faster and at a lower cost. This opens the way to the issue of synthesis of energy-absorber parameters with the desired energy-absorbing indicators. The conducted studies using neural networks also gave an answer to the question of the level of significance of a given parameter on the obtained indicators, as the same effect can be obtained by appropriately changing different geometrical parameters and position.

2. Crashworthiness indicators

Among the various indices for assessing structural crashworthiness, specific energy absorption (SEA) is commonly used to quantify the energy absorption capacity of different types of energy absorbers or different structural materials. It is the quotient of the energy absorbed and the mass of the energy absorber. The value of the absorbed energy EA is commonly obtained by determining the area under the crushing force-displacement (shortening) curve over a segment equal to the crushing distance. Since in the considerations carried out in this work a constant drop energy is assumed and the mass of all energy absorber models is identical - the SEA index loses its comparative aspect and is practically invariable for all columns considered and amounts to SEA= 14,617 kJ/kg. Besides, the EA and SEA energy values do not show by themselves whether the energy absorption process was effective, so the following indicators will be used in the considerations: PCF, MCF, CLE, SE and TE (abbreviations will be explained below). The initial peak crushing force PCF, occurring in the first milliseconds after impact, is an extremely important factor for biomechanical reasons and, therefore, a maximum reduction is sought at the design stage. Reducing this force is the simplest way to maximise the crash load efficiency index CLE, which is given by the formula:

$$CLE = \frac{MCF}{PCF} \cdot 100\% \quad (1)$$

Alternatively, it is defined as crash force efficiency CFE:

$$CFE = \frac{MCF}{PCF} \quad (1a)$$

Another crashworthiness indicator is stroke efficiency SE, which represents the deformation capacity of an absorber and it is defined as follows:

$$SE = \frac{U}{L_0} \quad (2)$$

where, U represents its maximum shortening (crushing distance) and L_0 its initial length.

The most desirable value of the SE factor is the highest, corresponding to the highest value of the crushing distance. The optimum structure during the crushing process should be able to use its entire available length to absorb the impact energy, obviously if the impact energy is large enough to cause such a large deformation. This is why SE is one of the basic indicators of crushing performance. A combination of the CLE (CFE) and the stroke efficiency SE was proposed by Hanssen et al. [17] as total efficiency TE to assess the whole performance of an energy absorber. This can be a percentage or a dimensionless value depending on whether the factor is CFE or CLE, as shown below:

$$TE = CLE \times SE \quad [\%] \quad (3)$$

$$TE = CFE \times SE \quad [-] \quad (3a)$$

4. Subject of the investigation

The subjects of the study were thin-walled aluminum tubes of square section with four dents formed by cylindrical embossing at the corners on each tube. All tube models are characterized by the cross-sectional dimensions 40×1.2 and the constant height $l=200$ mm. The dent's geometry was described by the diameter D and the depth g which

can easily be related to the overall dimension of the column section, while the position of the trigger is defined by the dimension h , which is the distance of its centre plane from the bottom edge as shown in Figure 1.

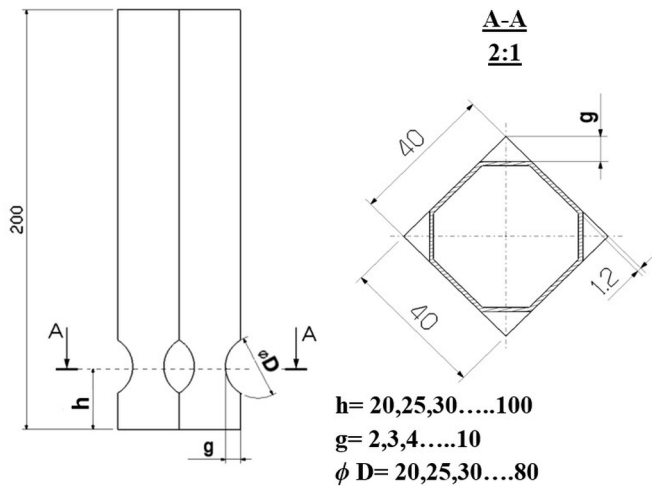


Fig. 1. Construction drawing of the column model with cross-section in the trigger location plane

The research program included the realization of a series of models differing in geometrical parameters of dent and its position. In the first round of research, a total of 103 models were numerically analyzed in order to obtain not only results, but above all data to create a neural network and predict the behavior and energy absorption capacity for any data configuration (D, g, h). The range of diameters of dent D was from 20 to 80 mm (50-200% of column width) and its depth g from 2 to 10 mm (5-25% of column width). The trigger position h ranged from 20 mm to 100 mm (mid surface) measured from the bottom edge. The following model designation has been adopted: the first letter denotes the type of trigger D (dent), then the subsequent dash gives the diameter of the trigger D , its depth g and its position h preceded by the letter h . For example, a model with a trigger diameter of 40 mm and a depth of 8 mm placed at a height of 30 mm was designated D-40-8-h30.

5. FE model

An analysis of the crushing behavior of the tested columns was carried out using FEM simulations. The Abaqus 2019 code of the Explicit method was used. The model of the thin-walled column with an embossment was made directly in the Part module (Figure 2a), instead of importing the geometry from Catia v5 system, as it was the case in previous publications [14, 15]. This approach allows, by editing the sketch, to quickly modify the geometric parameters, which

significantly reduces the time needed to perform subsequent structural variations, as shown in Figure 2b.

During the development of the FE model, this column was placed between two rigid plates, to which its edges were connected by means of *Tie* bonds. At the geometric centers of the plates, reference points RP were created, where the impact force (at the bottom point) and acceleration, velocity, displacement (at the top point) were recorded during the numerical simulation. The assembly model with reference points is shown in Figure 3a, and with the mesh created using 4-node shell elements S4R in Figure 3b. It can also be seen that a partitioning technique was used to create a uniformly divided mesh.

The contact domain was set up as the *General Contact* option (all with self). In the tangential plane, the contact properties of *Penalty type* were assumed, with a coefficient of friction equal to 0.2. The behaviour in the normal plane was declared as the *Hard Contact* option. On the lower rigid plate all degrees of freedom were disabled, while on the upper plate, which takes the impact, only displacement in the vertical direction was allowed.

The column was subjected to an impact load with a kinetic energy of $E = 1.47$ kJ corresponding to a mass of $m = 60$ kg falling with an initial velocity of $V_0 = 7$ m/s. Since the research program included experimental validation of the model, the properties of the EN AW6063-T6 material from which the column is made were determined by static tensile testing of samples cut from the profile by waterjet. The

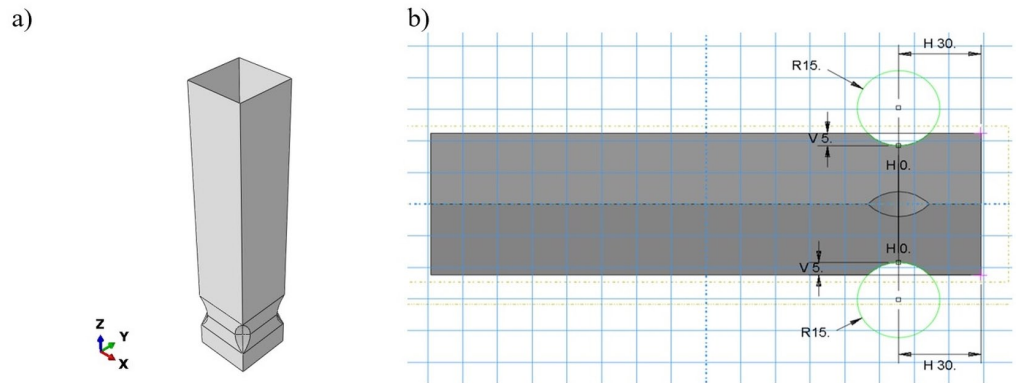


Fig. 2. FE model a) Column model with trigger on example of D-40-5-h30 model b) Modifiable sketch of trigger position and its geometrical parameters

material properties obtained in this way is shown in Table 1. Since aluminum alloys do not exhibit a significant sensitivity to the strain rate [39], a tri-linear material model was applied, neglecting the effect of the strain rate yet taking account of strain hardening. Constitutive relation does not cover the failure criterion. The numerical analysis of column crushing was carried out in two stages. In the first stage, a buckling analysis was carried out which resulted in buckling modes, of which the first will be needed for further computations. In the second stage, a non-linear geometrical problem of impact with a rigid plate of given energy is analysed, where the first buckling mode, according to which the real structure behaves, is implemented as a geometrical imperfection by means of special procedure. The omission of this procedure would lead to results of the deformation form, and therefore of the other results, significantly deviating from the reality represented by the experiment. The first mode of column buckling is shown in Figure 3c.

Table 1. Mechanical properties of aluminum alloy AW6063-T6

Tri-linear characteristic				Elongation [-]
Young's Modulus E [MPa]	70 000	Yield Strength σ_Y [MPa]	200	0
Density ρ [kg/m ³]	2 700		249.5	0.00248
Poisson's ratio ν [-]	0.33	Ultimate tensile strength σ_{ult} [MPa]	271.8	0.0598

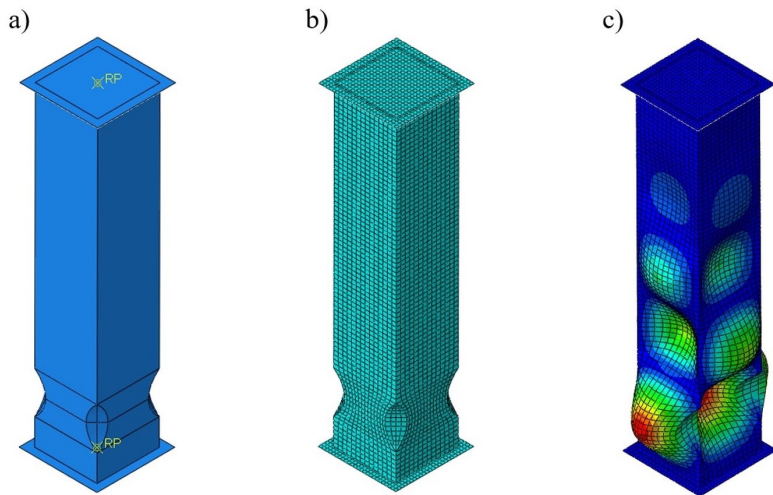


Fig. 3. FE model a) Assembly view with rigid plates and reference points b) with mesh c) first buckling mode

6. Experimental verification of numerical model

Impact tests were carried out using an Instron CEAST 9350HES drop hammer rig, a general view of which is shown in Figure 4a. Specimen D-40-6-h30 was selected for verification testing, and their designation was extended to include the S1,S2,S3 end. The columns were plugged at the ends by attaching cubes with holes for air evacuation during the crushing process. The column and cubes were mounted on measuring table equipped with a piezoelectric force sensor as can be seen in Figure 4b. The specimens were made from standard aluminum extrusions with square cross-section of 40 mm × 40 mm and wall thickness of 1.2 mm by cold stamping of their edges using a hydraulic press and an instrumentation - a special die consisting of a divided inner part, an outer part and punch, which is shown in Figure 4c.

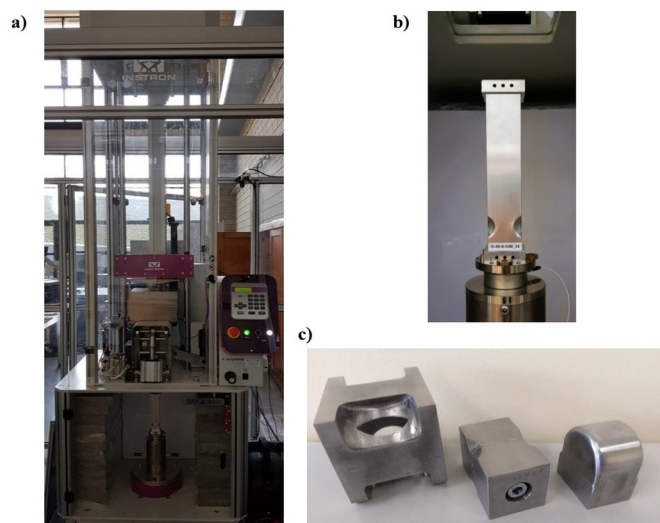


Fig. 4. Investigation and manufacture of triggered columns (a) General view of the drop hammer rig (Instron CEAST 9350HES) (b) Specimen D-40-6-h30_S1 mounted on a test bench (c) Instrumentation for making dents

Table 2. Crashworthiness indicators obtained from experiment and FEM simulation, comparison

Model	EA [J]	U3 _{MAX} [mm]	MCF [kJ]	PCF [kJ]	CLE [%]	SE [-]	TE [%]
D-40-6-h30_S1	1484,656	105,80	14,0324	45,0554	31,14	0,5290	16,48
D-40-6-h30_S2	1475,578	104,85	14,0739	43,5271	32,33	0,5242	16,95
D-40-6-h30_S3	1480,098	106,99	13,8345	44,6539	30,98	0,5349	16,57
Experiment Mean Value	1480,111	105,88	13,9803	44,4121	31,49	0,5294	16,67
D-40-6-h30_FEM	1468,047	107,25	13,6877	43,1998	31,68	0,5363	16,99
Difference [%]*	0,82	1,30	2,09	2,73	0,63	1,30	1,95

* - in relation to experimental values

As a result of the tests carried out, the load-shortening characteristics were obtained, which are presented in Figure 5 together with the curve for model D-40-6-h30_FEM, obtained by FEM calculations. As can be seen, the waveforms obtained from the drop tower are very close to those obtained from the FEM simulation. This is also a result of validation procedures consisting mainly in a precise adjustment of the mesh density, the main purpose of which was to obtain a similar crush distance. Subsequent force peaks occur at similar deformation stages (similar displacement) and their number is identical as is the number of folds that form as a result of the impact. It also shows that the material model adopted is sufficient to represent well the phenomena occurring during the crush. The FEM model is reliable and gives a good description of reality in terms of characteristics. The deformation forms produced as a result of the impact, despite the apparent slight skewness of specimens S1 and S2, correspond very well to those obtained from the FEM calculations, as can be seen in Figure 6.

As a consequence, the quality of the model is also very good in terms of calculating the energy absorption indicators. Table 2 shows the results of the calculations, which were based on the characteristics mentioned above. The calculations for the experiment are based on three tests and have been averaged for comparison with the FEM results. Similar validation studies on a different machine and at a different drop energy have already been carried out and presented in the paper [15], however, the purpose of the present publication required them to be carried out again due to the change in material, column height and the higher drop energy that can be achieved on the machine the authors have in their possession. The relatively small discrepancies between the calculated values, shows that the developed FEM model can be the basis for extensive parametric analyses and gives credence to the conclusions that will be drawn from it. More comprehensive experimental studies are planned for other projects in the future.

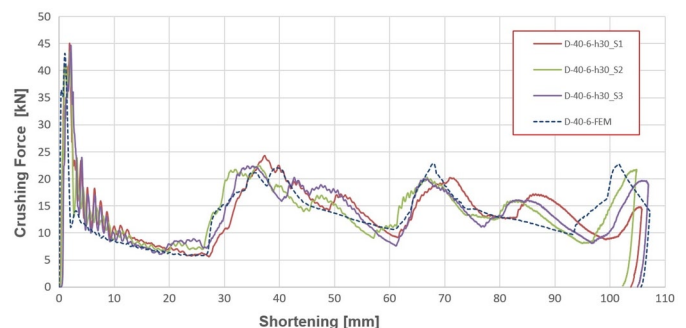


Fig. 5. Crushing force- shortening diagram obtained from experiment and FEM simulation for D-40-6-h30 models

7. Parametric study

Using the advanced and experimentally validated FE model, described in Chapter 5, by varying the geometric parameters of the crush initiator and its location, various model configurations were created and

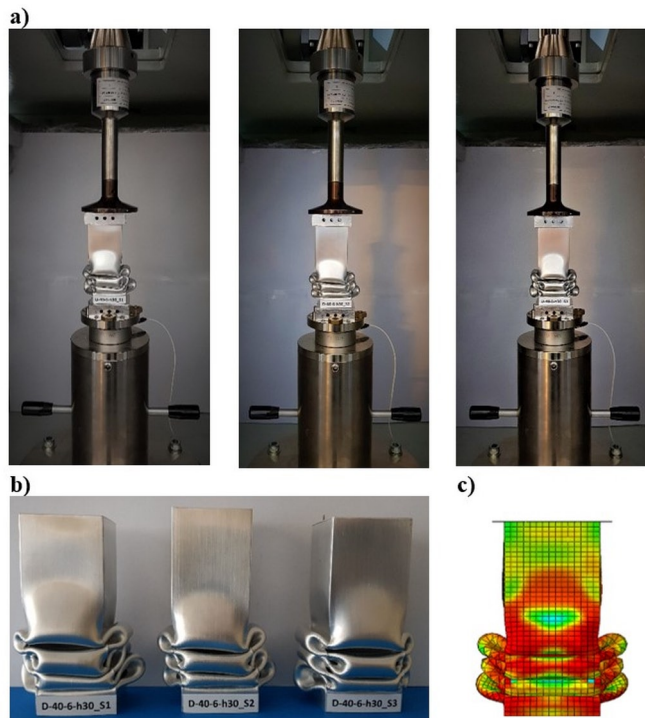


Fig. 6. Deformation forms of model D-40-6-h30 (a) deformed specimens just after the test (b) comparison of deformed specimens (c) deformation shape of the FEM model

subjected to numerical simulation of an impact with an energy corresponding to the experiment, in order to determine the crush force-shortening characteristic, which in turn is the basis for determining the energy absorption indicators. Examples of this type of characteristic are shown in Figure 7, with the results presented for a fixed trigger position relative to the base, which is $h=30$ mm. The individual curves present the results according to a certain key, showing how changing the diameter of the cylindrical embossment influences the curves at a certain embossment depth.

The calculated indicators for this group of models are presented in Table 3. It can easily be seen that the key parameter is the embossing depth, while its diameter is of significance, but much smaller. The value of the crush initiation force PCF is practically determined by the embossing depth. It can be seen not only in the table, but also by analysing successive diagrams (Figure 7), where the value of PCF decreases with increasing embossing depth, while within individual diagrams PCF remains practically constant with little dependence on embossing diameter. It can also be seen from the graphs that in the initial phase of the crush, when the thin-walled structure disturbed by the presence of the trigger is deformed under impact, the value of shortening accompanying the transition of the structure to the phase of forming the first fold increases with the increase of the diameter of the embossing at constant depth. This is very well seen in particular in Figure 7c. The amount of energy absorbed in this crushing phase of the structure is therefore quite varied and affects the subsequent behaviour of the structure.

The minimisation of the PCF force is critical to maximise the value of the CLE index, as the MCF varies little with the change in trigger

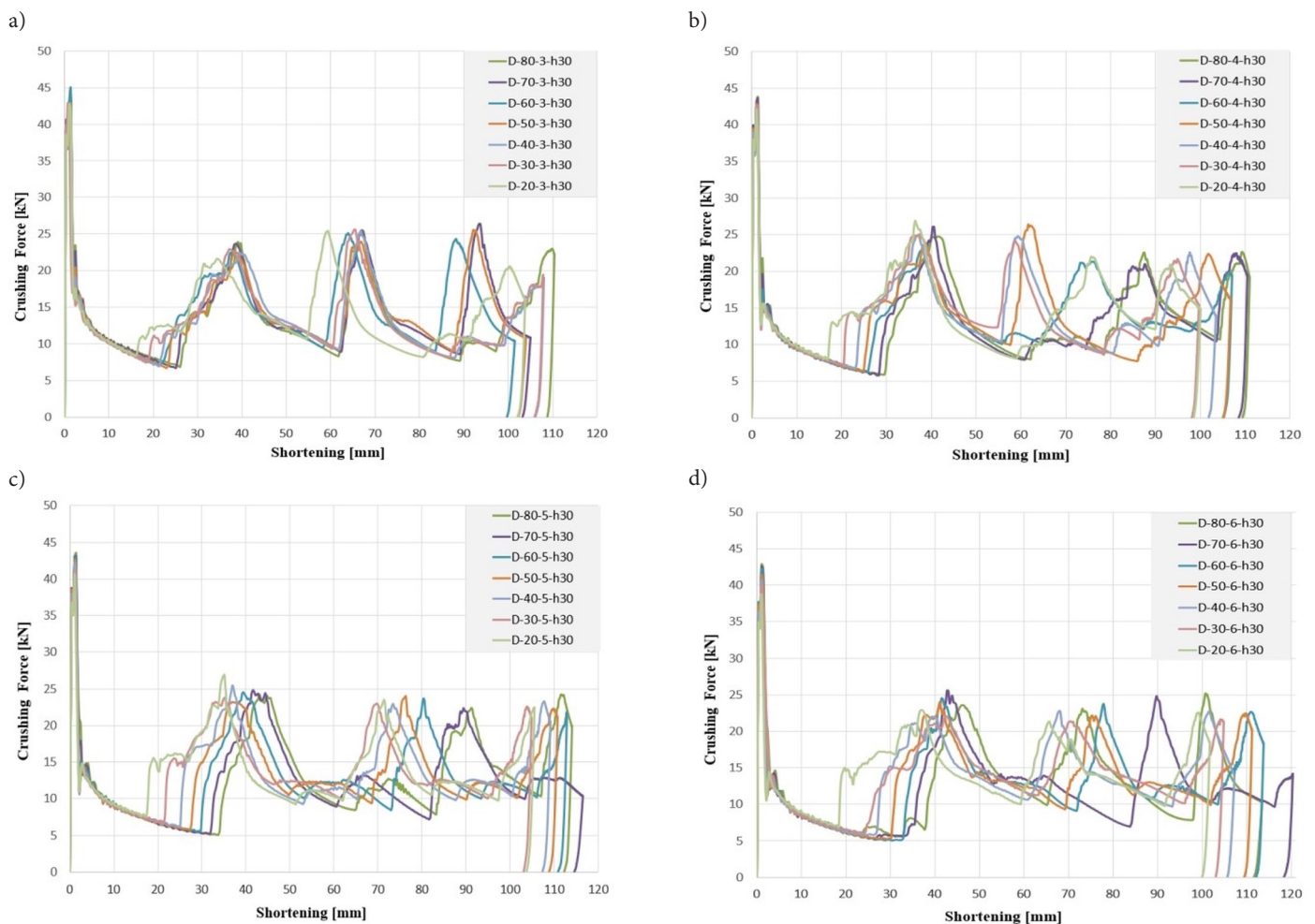


Fig. 7. Crushing force vs shortening diagrams obtained for columns with different trigger geometric parameters and constant trigger position. The individual graphs refer to the changing depth of the trigger for different dents' diameters: a) $D=20-80$ mm, $g=3$ mm, $h=30$ mm, b) $D=20-80$ mm, $g=4$ mm, $h=30$ mm, c) $D=20-80$ mm, $g=5$ mm, $h=30$ mm, d) $D=20-80$ mm, $g=6$ mm, $h=30$ mm

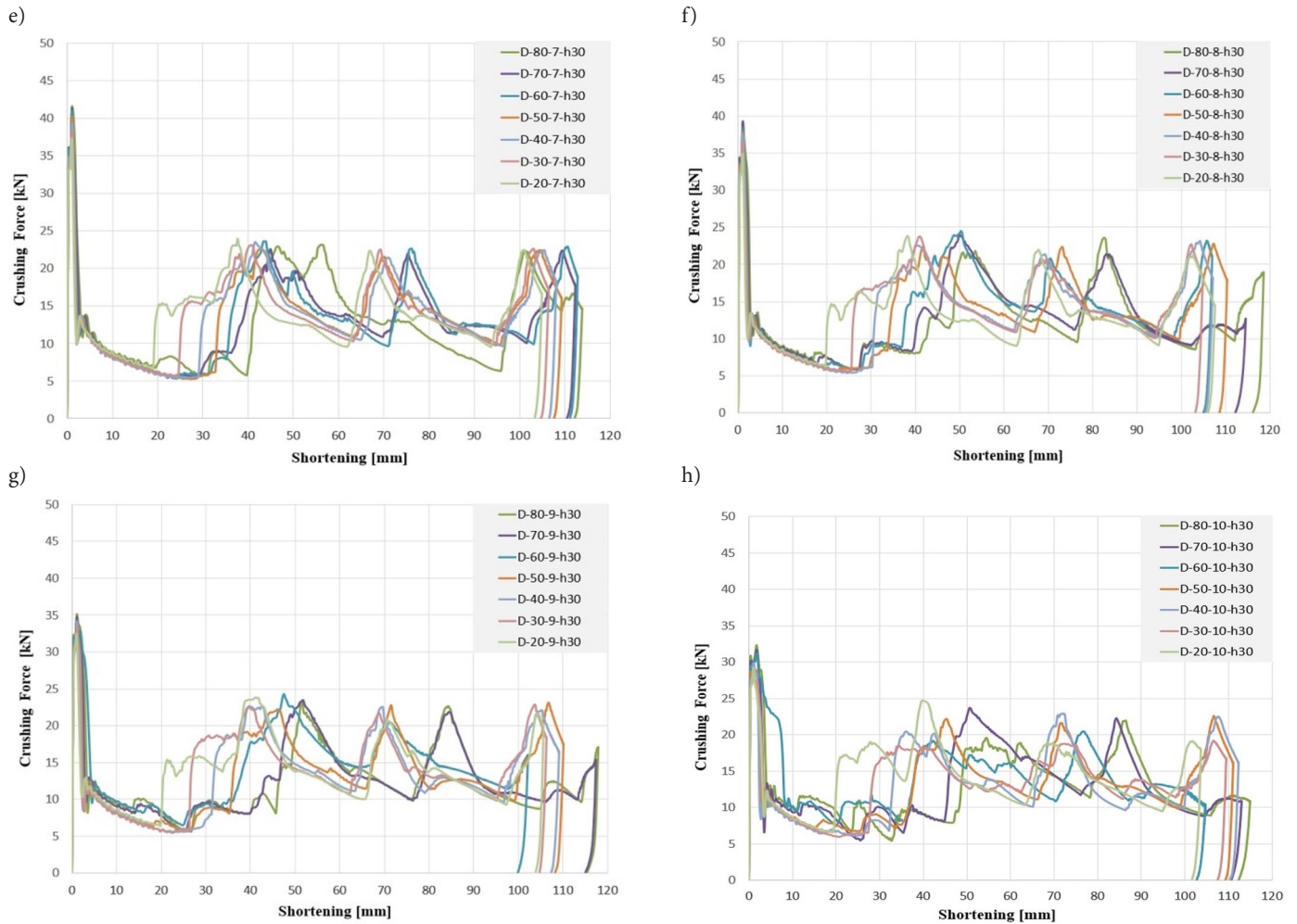


Fig. 7. (cont.) Crushing force vs shortening diagrams obtained for columns with different trigger geometric parameters and constant trigger position. The individual graphs refer to the changing depth of the trigger for different dents' diameters: e) $D=20-80$ mm, $g=7$ mm, $h=30$ mm, f) $D=20-80$ mm, $g=8$ mm, $h=30$ mm, g) $D=20-80$ mm, $g=9$ mm, $h=30$ mm, h) $D=20-80$ mm, $g=10$ mm, $h=30$ mm

Table 3. Crashworthiness indicators obtained from FEM numerical calculations for specific trigger geometric parameters - Part 1 (fixed trigger position $h=30$ mm, its diameter D and depth g are varied)

No	Model Designation	D [mm]	g [mm]	h [mm]	PCF [kN]	MCF [kN]	CLE [%]	SE [-]	TE [%]
1	D-20-2-h30	20	2	30	47,084	12,952	27,507	0,5669	15,595
2	D-20-3-h30	20	3	30	45,636	14,124	30,949	0,5196	16,082
3	D-20-4-h30	20	4	30	43,877	14,678	33,454	0,4999	16,724
4	D-20-5-h30	20	5	30	41,457	13,903	33,537	0,5277	17,697
5	D-20-6-h30	20	6	30	39,513	14,412	36,475	0,5089	18,562
6	D-20-7-h30	20	7	30	37,211	13,967	37,533	0,5250	19,706
7	D-20-8-h30	20	8	30	34,664	13,637	39,342	0,5380	21,165
8	D-20-9-h30	20	9	30	32,317	13,873	42,927	0,5287	22,696
9	D-20-10-h30	20	10	30	29,381	14,152	48,168	0,5185	24,975
10	D-30-2-h30	30	2	30	47,537	13,339	28,060	0,5505	15,456
11	D-30-3-h30	30	3	30	45,940	13,595	29,593	0,5396	15,968
12	D-30-4-h30	30	4	30	44,467	14,711	33,084	0,4988	16,501
13	D-30-5-h30	30	5	30	42,271	13,988	33,091	0,5243	17,350
14	D-30-6-h30	30	6	30	40,897	13,978	34,179	0,5247	17,934
15	D-30-7-h30	30	7	30	40,897	13,776	33,685	0,5323	17,929
16	D-30-8-h30	30	8	30	36,308	13,966	38,466	0,5249	20,191
17	D-30-9-h30	30	9	30	33,389	13,789	41,298	0,5317	21,958

18	D-30-10-h30	30	10	30	30,140	13,423	44,535	0,5476	24,388
19	D-40-2-h30	40	2	30	47,567	13,123	27,588	0,5601	15,451
20	D-40-3-h30	40	3	30	46,233	13,569	29,348	0,5406	15,867
21	D-40-4-h30	40	4	30	45,123	14,185	31,437	0,5171	16,256
22	D-40-5-h30	40	5	30	43,200	13,443	31,119	0,5459	16,988
23	D-40-6-h30	40	6	30	41,152	13,688	33,262	0,5363	17,837
24	D-40-7-h30	40	7	30	39,516	13,572	34,345	0,5407	18,570
25	D-40-8-h30	40	8	30	37,758	13,682	36,236	0,5361	19,425
26	D-40-9-h30	40	9	30	34,100	13,441	39,416	0,5456	21,505
27	D-40-10-h30	40	10	30	30,958	13,046	42,141	0,5619	23,678
28	D-50-2-h30	50	2	30	47,599	13,481	28,322	0,5468	15,486
29	D-50-3-h30	50	3	30	46,506	14,118	30,357	0,5197	15,778
30	D-50-4-h30	50	4	30	45,222	13,751	30,408	0,5334	16,218
31	D-50-5-h30	50	5	30	43,493	13,254	30,474	0,5536	16,871
32	D-50-6-h30	50	6	30	42,108	13,194	31,334	0,5561	17,426
33	D-50-7-h30	50	7	30	40,316	13,428	33,306	0,5463	18,195
34	D-50-8-h30	50	8	30	37,891	13,292	35,080	0,5519	19,360
35	D-50-9-h30	50	9	30	34,221	13,320	38,924	0,5505	21,427
36	D-50-10-h30	50	10	30	31,633	13,195	41,713	0,5558	23,183
37	D-60-2-h30	60	2	30	47,597	13,370	28,089	0,5496	15,438
38	D-60-3-h30	60	3	30	46,378	14,467	31,194	0,5073	15,824
39	D-60-4-h30	60	4	30	45,130	13,705	30,367	0,5352	16,251
40	D-60-5-h30	60	5	30	43,954	12,999	29,574	0,5645	16,695
41	D-60-6-h30	60	6	30	42,560	12,894	30,295	0,5693	17,248
42	D-60-7-h30	60	7	30	41,185	13,008	31,583	0,5639	17,810
43	D-60-8-h30	60	8	30	38,553	13,700	35,535	0,5352	19,018
44	D-60-9-h30	60	9	30	36,382	14,354	39,453	0,5110	20,159
45	D-60-10-h30	60	10	30	32,490	14,002	43,096	0,5239	22,577
46	D-70-2-h30	70	2	30	47,574	13,279	27,912	0,5533	15,445
47	D-70-3-h30	70	3	30	46,589	13,982	30,011	0,5251	15,757
48	D-70-4-h30	70	4	30	45,332	13,288	29,313	0,5522	16,187
49	D-70-5-h30	70	5	30	44,327	12,608	28,443	0,5827	16,575
50	D-70-6-h30	70	6	30	43,039	12,210	28,369	0,6016	17,067
51	D-70-7-h30	70	7	30	41,237	13,057	31,662	0,5620	17,795
52	D-70-8-h30	70	8	30	39,686	12,814	32,288	0,5727	18,492
53	D-70-9-h30	70	9	30	36,262	12,497	34,462	0,5875	20,246
54	D-70-10-h30	70	10	30	33,020	12,990	39,340	0,5647	22,216
55	D-80-2-h30	80	2	30	47,579	13,474	28,320	0,5452	15,440
56	D-80-3-h30	80	3	30	46,639	13,292	28,500	0,5520	15,733
57	D-80-4-h30	80	4	30	45,530	13,221	29,038	0,5551	16,118
58	D-80-5-h30	80	5	30	44,644	12,872	28,832	0,5701	16,437
59	D-80-6-h30	80	6	30	43,581	12,939	29,690	0,5673	16,843
60	D-80-7-h30	80	7	30	41,973	12,883	30,694	0,5695	17,479
61	D-80-8-h30	80	8	30	39,730	12,378	31,156	0,5927	18,467
62	D-80-9-h30	80	9	30	36,995	12,443	33,635	0,5895	19,827
63	D-80-10-h30	80	10	30	34,144	12,772	37,407	0,5745	21,490

Table 4. Crashworthiness indicators obtained from FEM numerical calculations for specific trigger geometric parameters- Part 2 (fixed trigger diameter $D=40$ mm, its depth g and position h are varied)

No	Model Designation	D [mm]	g [mm]	h [mm]	PCF [kN]	MCF [kN]	CLE [%]	SE [-]	TE [%]
1	D-40-2-h20	40	2	20	47,768	13,305	27,853	0,5509	15,345
2	D-40-2-h30	40	2	30	47,567	13,123	27,588	0,5601	15,451
3	D-40-2-h40	40	2	40	47,832	13,364	27,939	0,5484	15,322
4	D-40-2-h50	40	2	50	48,522	13,099	26,996	0,5593	15,099
5	D-40-2-h60	40	2	60	48,838	13,748	28,150	0,5328	14,998
6	D-40-2-h70	40	2	70	48,847	14,092	28,849	0,5203	15,009
7	D-40-2-h80	40	2	80	48,635	14,395	29,598	0,5093	15,075
8	D-40-2-h90	40	2	90	48,984	14,574	29,753	0,5032	14,971
9	D-40-2-h100	40	2	100	49,264	14,845	30,134	0,4937	14,878
10	D-40-4-h20	40	4	20	45,416	12,827	28,243	0,5714	16,138
11	D-40-4-h30	40	4	30	45,123	14,185	31,437	0,5171	16,256
12	D-40-4-h40	40	4	40	44,656	13,539	30,318	0,5412	16,410
13	D-40-4-h50	40	4	50	45,242	14,494	32,037	0,5056	16,197
14	D-40-4-h60	40	4	60	46,608	13,429	28,813	0,5453	15,711
15	D-40-4-h70	40	4	70	47,464	13,739	28,946	0,5333	15,436
16	D-40-4-h80	40	4	80	47,694	13,787	28,907	0,5313	15,358
17	D-40-4-h90	40	4	90	47,982	13,476	28,086	0,5436	15,266
18	D-40-4-h100	40	4	100	48,573	13,522	27,839	0,5418	15,082
19	D-40-6-h20	40	6	20	41,533	13,522	32,557	0,5347	17,409
20	D-40-6-h30	40	6	30	41,152	13,688	33,262	0,5363	17,837
21	D-40-6-h40	40	6	40	41,340	13,522	32,709	0,5516	18,043
22	D-40-6-h50	40	6	50	41,909	13,522	32,265	0,5577	17,996
23	D-40-6-h60	40	6	60	42,358	13,522	31,923	0,5480	17,493
24	D-40-6-h70	40	6	70	42,502	13,522	31,815	0,5534	17,608
25	D-40-6-h80	40	6	80	42,563	13,522	31,769	0,5666	17,999
26	D-40-6-h90	40	6	90	42,927	13,522	31,500	0,5612	17,678
27	D-40-6-h100	40	6	100	43,653	13,522	30,976	0,5600	17,346
28	D-40-8-h20	40	8	20	36,941	12,649	34,241	0,5797	19,851
29	D-40-8-h30	40	8	30	37,758	13,682	36,236	0,5361	19,425
30	D-40-8-h40	40	8	40	37,026	12,599	34,027	0,5818	19,798
31	D-40-8-h50	40	8	50	39,158	12,986	33,163	0,5630	18,671
32	D-40-8-h60	40	8	60	39,993	13,209	33,028	0,5545	18,315
33	D-40-8-h70	40	8	70	40,164	12,843	31,976	0,5692	18,202
34	D-40-8-h80	40	8	80	40,321	12,722	31,552	0,5763	18,184
35	D-40-8-h90	40	8	90	40,395	12,838	31,781	0,5717	18,170
36	D-40-8-h100	40	8	100	40,526	12,995	32,066	0,5643	18,095
37	D-40-10-h20	40	10	20	31,032	13,188	42,498	0,5564	23,646
38	D-40-10-h30	40	10	30	30,958	13,046	42,141	0,5619	23,678
39	D-40-10-h40	40	10	40	31,137	12,589	40,431	0,5826	23,557
40	D-40-10-h50	40	10	50	35,219	12,799	36,341	0,5731	20,828
41	D-40-10-h60	40	10	60	36,485	12,876	35,291	0,5696	20,102
42	D-40-10-h70	40	10	70	36,633	12,777	34,878	0,5733	19,997
43	D-40-10-h80	40	10	80	36,804	12,490	33,937	0,5872	19,927
44	D-40-10-h90	40	10	90	39,109	12,928	33,056	0,5674	18,757
45	D-40-10-h100	40	10	100	39,010	12,866	32,981	0,5704	18,812

Table 5. Crashworthiness indicators obtained from FEM numerical calculations for specific trigger geometric parameters- Part 3 (other configurations)

No	Model Designation	D [mm]	g [mm]	h [mm]	PCF [kN]	MCF [kN]	CLE [%]	SE [-]	TE [%]
1	D-20-2-h20	20	2	20	47,884	13,463	28,115	0,5428	15,261
2	D-20-3-h100	20	2	100	49,331	14,493	29,379	0,5086	14,943
3	D-20-6-h60	20	6	60	42,124	13,841	32,858	0,5326	17,501
4	D-20-10-h20	20	10	20	28,956	13,459	46,480	0,5461	25,382
5	D-20-10-h100	20	10	100	39,195	13,730	35,031	0,5260	18,427
6	D-40-10-h20	40	10	20	30,982	13,244	42,747	0,5558	23,757
7	D-40-10-h80	40	10	80	38,145	13,014	34,118	0,5662	19,317
8	D-60-5-h80	60	5	80	47,061	12,989	27,601	0,5676	15,666
9	D-60-7-h50	60	7	50	40,929	12,994	31,747	0,5671	18,003
10	D-80-2-h20	80	2	20	47,901	13,350	27,870	0,5521	15,386
11	D-80-2-h100	80	2	100	49,318	14,586	29,575	0,5054	14,946
12	D-80-6-h60	80	6	60	44,499	12,337	27,724	0,5978	16,574
13	D-80-10-h20	80	10	100	39,555	13,396	33,867	0,5509	18,656

depth. The highest energy-absorbing CLE indicators are obtained for maximum embossing depth and minimum embossing diameter.

In order to broaden the base of results, which is necessary due to the quality of the neural network being built and its predictive capabilities, further design variations of the energy absorbers were modelled and numerical calculations were carried out according to an identical procedure. The results of these calculations are shown in Table 4, where the results are given for a fixed trigger diameter and the depth of the embossing and its position (in the range up to 100 mm) was changed. The next Table 5 contains the results of models characterized by mostly boundary geometric parameter values. Obtaining these data significantly improved the prediction quality of the network.

8. Multilayer perceptron networks study

Neural networks are signal processing mathematical models. The most popular structure of Artificial Neural Network is multilayer perceptron. This network model consists of numerous neurons set in layers. Regardless of the type, each neural network uses numerical input values and sets numerical output values.

In regression issues, the aim is to estimate the value of the continuous output variable. The values of PCF, CLE, SE, TE indicators from the numerical experiment are the values of output variables. Trigger parameters were taken as input variables. These are position (h), depth (g) and diameter (D), which are shown in Tables 3-5. These parameters are discussed in detail in Chapter 4.

Regression problems are represented by data sets, in which the output variable is numerical. Figure 8 shows one of the most frequently used activation functions used in the research - the logistic activation function.

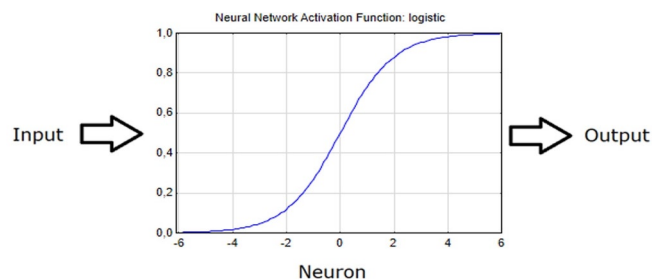


Fig. 8. Logistic activation function

This is an S-function. Output values bound between 0 and 1, normalizing the output of each neuron. This type of activation function enables clear predictions. For x above 2 or below -2, the prediction value is close to 1 or 0. The logistical function is smooth and easily differentiated, these features enable the network training algorithm to work.

The function can be represented by the equation:

$$u(x) = \frac{1}{1 + e^{-x}} \quad (4)$$

Two MLP neural networks were used in the numerical study. Based on preliminary experiments, it was decided to test networks with four and five neurons in the hidden layer. Table 6 lists the values of the training rates for the MLP networks with respect to predicted indicators.

The Broyden-Fletcher-Goldfarb-Shanno (BFGS) training method is a quasi-Newton method. In numerical optimization, the algorithm

Table 6. Artificial neural network operation parameters

Network	Quality			Training algorithm	Error function	Activation (Hidden)	Activation (Output)
	Training	Testing	Validation				
MLP 3-4-4	0,895826	0,904728	0,977966	BFGS 34	SOS	Logistic	Logistic
MLP 3-5-4	0,893355	0,892867	0,977768	BFGS 27	SOS	Logistic	Logistic

Table 7. Networks sensitivity (training set)

Network	Diameter D	Depth g	Position h
MLP 3-4-4	2,364994	17,73557	4,105513
MLP 3-5-4	2,262062	17,07618	3,951909
Mean value	2,313528	17,40587	4,028711

Table 8. Correlation rates

	PCF			CLE			SE			TE		
	Training	Testing	Validation									
MLP 3-4-4	0,98828	0,99415	0,99515	0,94571	0,97153	0,99600	0,66706	0,66181	0,92606	0,98225	0,99143	0,99466
MLP 3-5-4	0,98645	0,98932	0,99428	0,94480	0,97031	0,99385	0,66068	0,62273	0,92870	0,98150	0,98913	0,99424

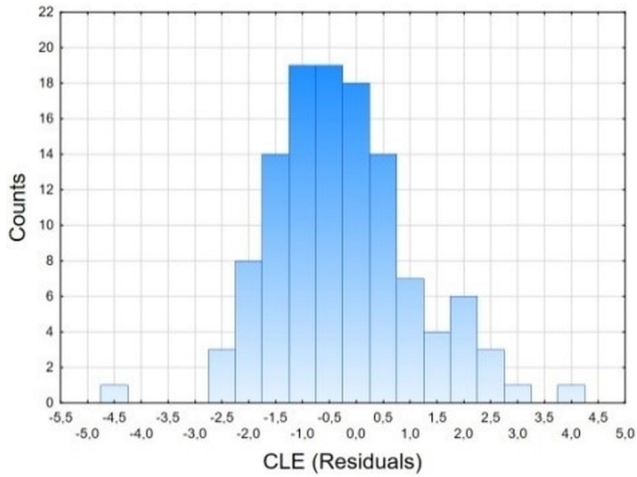


Fig. 9. Residual analysis for the CLE parameter

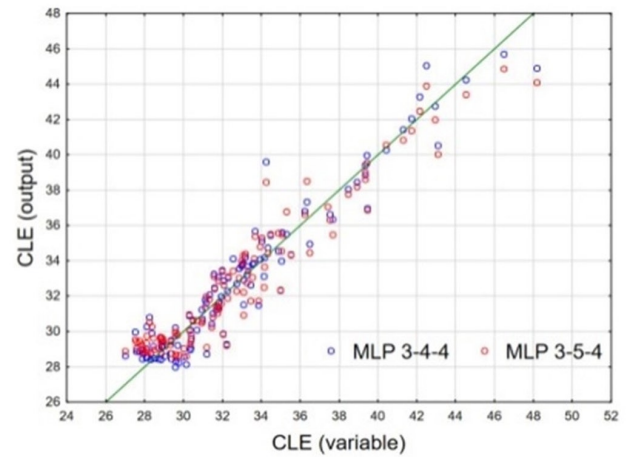


Fig. 12. Analysis of the forecast to the observed value for the indicator

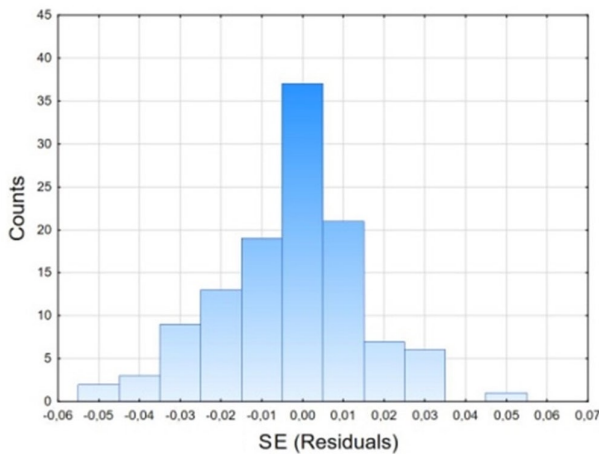


Fig. 10. Residual analysis for the SE parameter

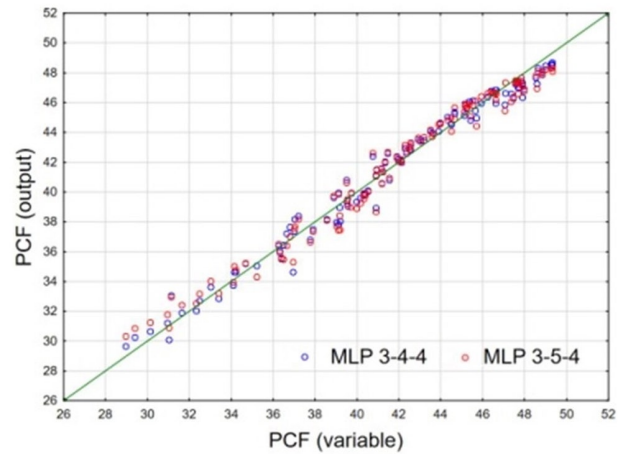


Fig. 13. Analysis of the forecast to the observed value for the indicator

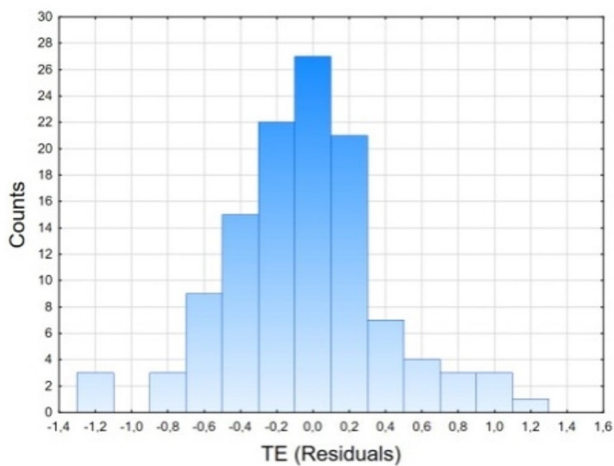


Fig. 11. Residual analysis for the TE parameter

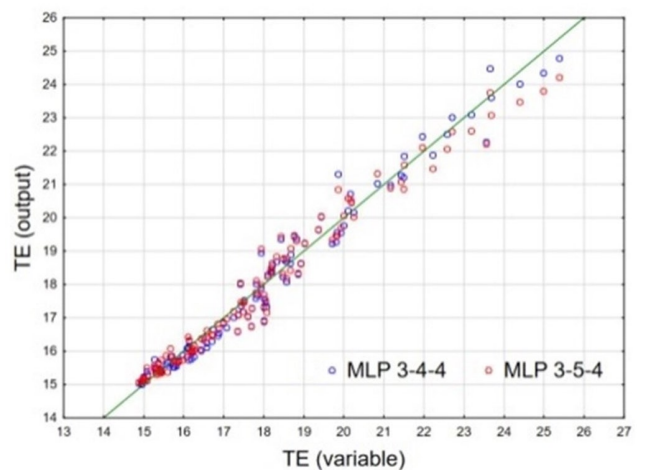


Fig. 14. Analysis of the forecast to the observed value for the indicator

BFGS is an iterative method for solving non-linear optimization problems. The error function is the sum of the squares (SOS) of the deviations between the reference value and the network output.

The sensitivity analysis shows that the depth of the trigger is the most important parameter (Table 7). Another important parameter is the position of the initiator. The least important is the diameter of the dent.

The parameters of neural models, except SE, show high correlation for all datasets: training, testing and validation (Table 8).

It is worthwhile to examine the distribution of the residuals, i.e. the differences between the output variable and its prediction (Figures 9-11).

For both active networks, the histograms indicate that the residuals are more or less normally distributed around zero, which is in line with the general assumption of normal noise in the data. Wider histograms indicate more noise. A histogram that is too narrow compared to the amount of noise in the data would indicate that the network is overfitting. Histogram examination shows that the residues are close to normal distribution with a zero average.

It is a good indication that the network has discovered the assumed noise model. We assume that noise on the target variables is normally distributed with zero mean and an unknown variance.

Figures 12-14 show the relationship of the results obtained by the neural network depending on the actual value. These graphs show the effectiveness of the two MLP networks analysed.

The figures 15-22 show the values of the analysed indicators depending on the geometric parameters and position of the trigger.

It can be seen from the above graphs that in some cases, it is possible to fit a surface plot representing the function of the dependence of the CLE, PCF, SE and TE parameters on the input geometric parameters.

Figures 15 and 17 show that especially changing the dent depth definitely affects the CLE, PCF, TE and SE parameters. The diameter of the trigger particularly influences the determination of the SE parameter.

Figures 16 and 18 indicate that a significant change in CLE and PCF indicators occurs with a high depth and low trigger position configuration.

9. Final conclusions

The conducted research has shown that artificial neural networks can be applied to predict the values of crashworthiness indicators with an acceptable error.

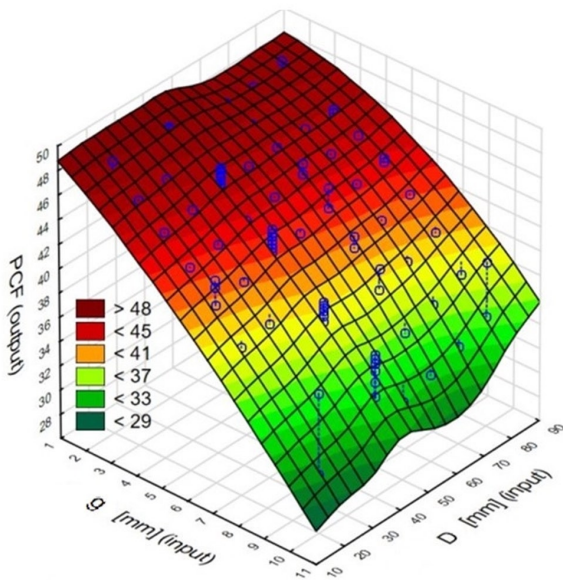


Fig. 15. PCF value as a function of depth g and diameter D

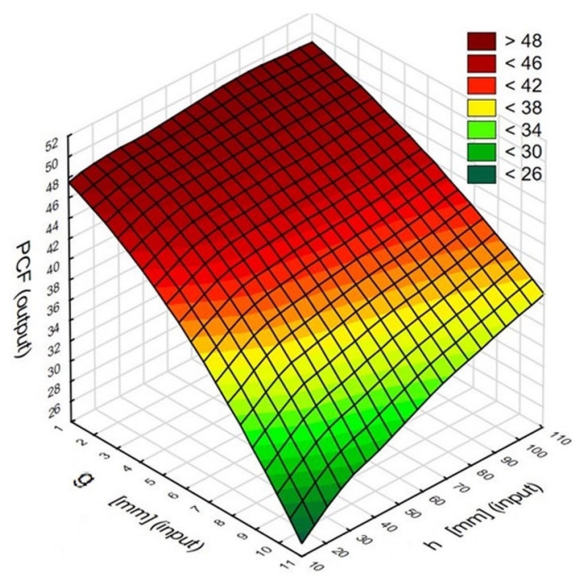


Fig. 16. PCF value as a function of depth g and position h

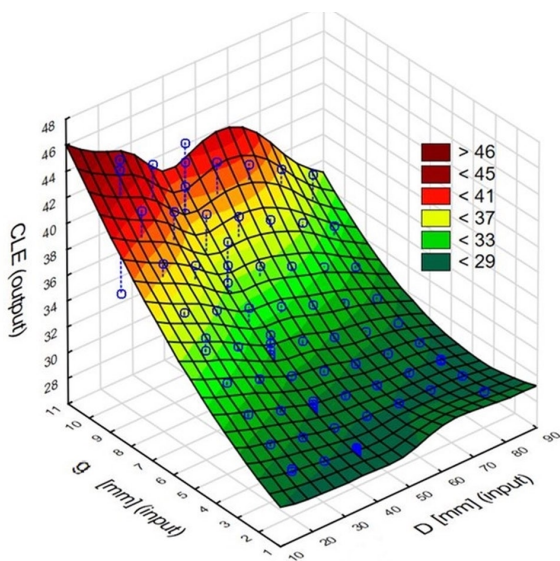


Fig. 17. CLE value as a function of depth g and diameter D

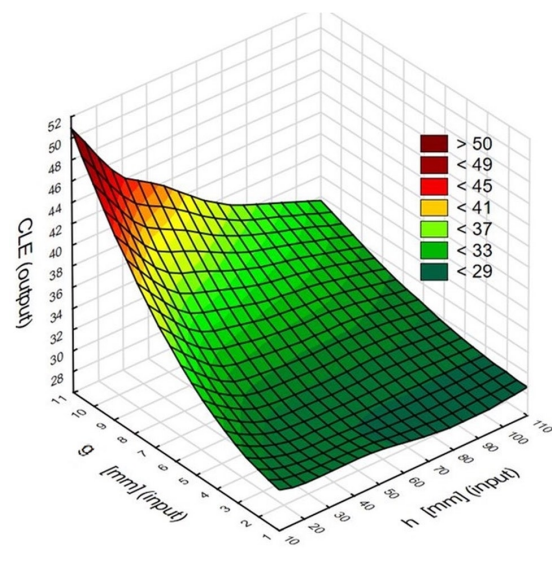


Fig. 18. CLE value as a function of depth g and position h

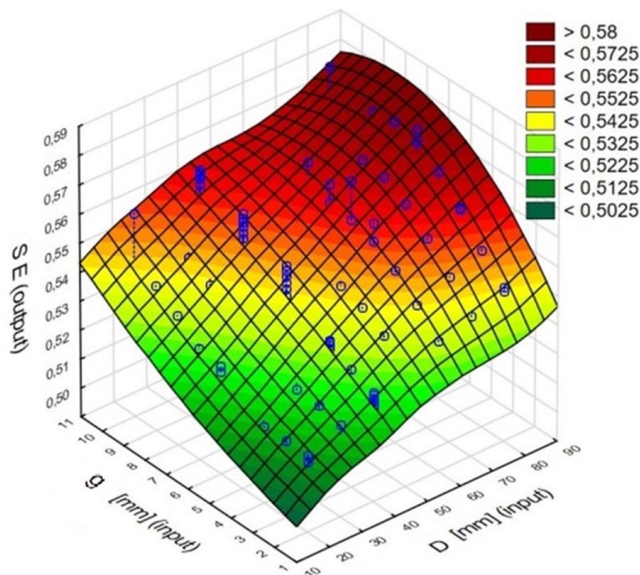


Fig. 19. SE value as a function of depth g and diameter D

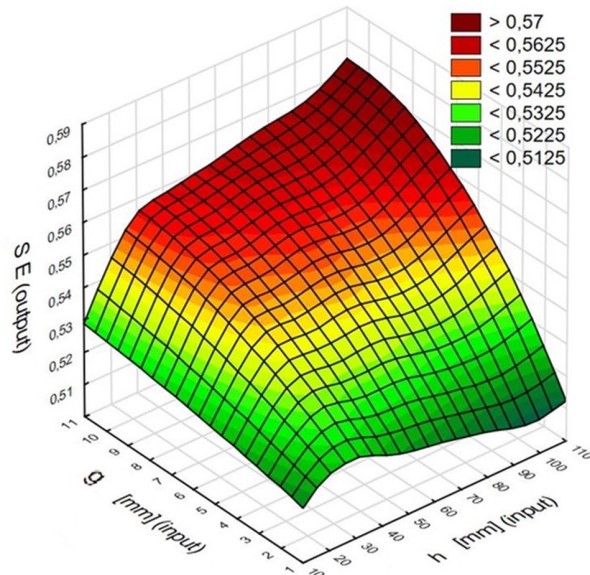


Fig. 20. SE value as a function of depth g and position h

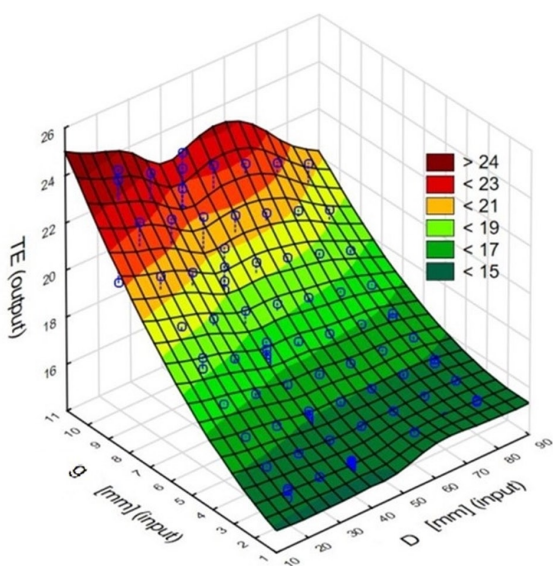


Fig. 21. TE value as a function of depth g and diameter D

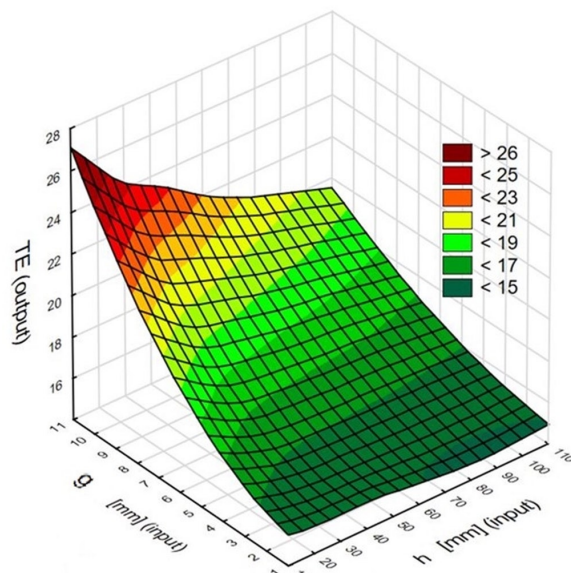


Fig. 22. TE value as a function of depth g and position h

There are minor differences between the network models studied. It is important to note that the simpler the model the faster it operates. Quality differences between networks with four and five neurons in the hidden layer are below 2% (Table 6).

From the network sensitivity analysis it can be concluded that by far the most important parameter for the performance of the model is the trigger depth. The position of the trigger and the diameter affect the performance of the MLP to a lesser extent. This conclusion should be taken into account when designing energy-absorbing models.

The overall quality of the network performance was about 90% for the training set and over 97% for the test data. The correlation coefficients indicate that the SE coefficient was the most difficult to predict. For the PCF, CLE and TE coefficients the prediction quality was 95-99% (Table 8).

In order to confirm the universality of the neural network performance, an additional numerical experiment was introduced. The random models, including two with parameters outside the range that was used to training the ANN were tested (D-80-4-h140, D-100-8-h50). Figure 23 shows the crushing force-shortening characteristics and Table 9 shows the indicator results for the random test specimens.

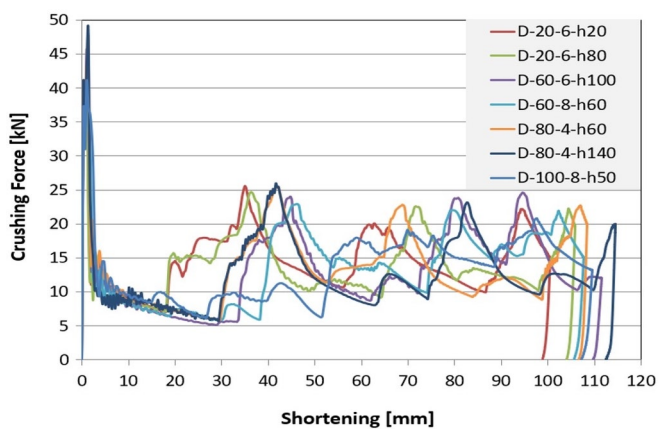


Fig. 23. Crushing force vs shortening diagrams obtained for testing models

Predictions of indicators were then made for the test specimens and their values were compared with the results obtained by the FE

Table 9. Crashworthiness indicators obtained for testing models from FE simulations

Designation	PCF [kN]	MCF [kN]	CLE [%]	SE [-]	TE [%]
D-20-6-h20	38,898	14,657	37,680	0,5022	18,923
D-20-6-h80	40,751	13,915	34,148	0,5293	18,074
D-60-6-h100	45,712	13,191	28,857	0,5580	16,103
D-60-8-h60	39,416	13,190	33,461	0,5388	18,859
D-80-4-h60	47,370	13,597	28,703	0,5422	15,563
D-80-4-h140	48,918	12,861	26,291	0,5721	15,040
D-100-8-h50	41,058	13,442	32,739	0,5472	17,915

slightly exceed 4,8%. Good prediction properties are shown by both networks when it comes to the calculation of TE, which is after all the product of SE and CLE, despite the relatively high differences obtained in the prediction of individual factors. This is because these factors are predicted most often simultaneously with over- and under-estimates.

As a practical aspect of the research carried out, it should be emphasised that the use of multilayer perceptron can successfully speed up the design process.

The study carried out, although it concerns an energy absorber with a specific type of trigger, can be successfully extended to energy absorbers with other types of trigger, provided that it is characterised by several geometrical parameters whose interaction is difficult to grasp. As part of such work, a neural network is planned for an energy absorber with a trigger in the form of spheroidal embossments on the

Table 10. Crashworthiness indicators obtained from MLP 3-4-4 NN and relative error values in relation to FE simulation results

Relative error (difference)										
Designation	PCF [kN]	MCF [kN]	CLE [%]	SE [-]	TE [%]	Δ_{PCF} [%]	Δ_{MCF} [%]	Δ_{CLE} [%]	Δ_{SE} [%]	Δ_{TE} [%]
D-20-6-h20	39,434	14,355	36,243	0,5137	18,218	1,38	2,06	3,81	2,29	3,72
D-20-6-h80	42,000	13,780	32,753	0,5381	17,463	3,07	0,97	4,08	1,67	3,38
D-60-6-h100	45,965	13,275	29,894	0,5537	16,612	0,55	0,64	3,59	0,77	3,16
D-60-8-h60	39,838	12,918	32,502	0,5698	18,627	1,07	2,06	2,86	5,55	3,13
D-80-4-h60	47,196	13,141	28,558	0,5565	15,784	0,37	3,35	0,50	2,64	1,42
D-80-4-h140	48,718	13,508	28,027	0,5407	15,439	0,41	5,03	6,60	5,48	2,65
D-100-8-h50	42,603	12,568	29,946	0,5827	17,614	3,76	6,50	8,53	6,49	1,68

Table 11. Crashworthiness indicators obtained from MLP 3-5-4 NN and relative error values in relation to FE simulation results

Designation	PCF [kN]	MCF [kN]	CLE [%]	SE [-]	TE [%]	Δ_{PCF} [%]	Δ_{MCF} [%]	Δ_{CLE} [%]	Δ_{SE} [%]	Δ_{TE} [%]
D-20-6-h20	39,683	14,525	37,339	0,5053	18,644	2,02	0,90	0,91	0,62	1,48
D-20-6-h80	40,692	13,757	33,970	0,5351	18,099	0,14	1,14	0,52	1,09	0,14
D-60-6-h100	46,598	13,201	29,660	0,5588	15,956	1,94	0,08	2,78	0,15	0,91
D-60-8-h60	39,827	13,073	32,688	0,5632	18,421	1,04	0,89	2,31	4,34	1,99
D-80-4-h60	47,560	13,391	28,821	0,5504	15,556	0,40	1,51	0,41	1,51	0,04
D-80-4-h140	49,069	13,596	27,958	0,5445	15,022	0,31	5,71	6,34	4,83	0,12
D-100-8-h50	41,025	12,927	31,535	0,5695	17,911	0,08	3,83	3,68	4,07	0,03

method. The predicted indicator values along with the percentage difference from the FE calculations are shown in Tables 10 and 11.

In terms of predicting the PCF values, the maximum differences are found in the MLP-3-4-4 network and are about 3.75%, while for the MLP-3-5-4 network they are maximum 2%. Regarding the MCF and CLE indicator, the maximum differences in both networks were obtained for out-of-range specimens and are between 5-8.5%, where again the MLP 3-5-4 network had better prediction properties. The prediction of the SE indicator, also obtains maximum differences for out-of-range specimens. These differences are between 5.5 and 6.5% and apply to MLP3-4-4 networks, while for MLP3-5-4 networks they

lateral surfaces, where some results on experimentally validated numerical analysis have already been shown [16].

Acknowledgements

The project/research was financed in the framework of the Project Lublin University of Technology - Regional Excellence Initiative, funded by the Polish Ministry of Science and Higher Education (contract no. 030/RID/2018/19).

References

1. Abbasi M, Reddy S, Ghafari-Nazari A, Fard M. Multiobjective crashworthiness optimization of multi-cornered thin-walled sheet metal members. *Thin-Walled Structures* 2015. doi:10.1016/j.tws.2014.12.009, <https://doi.org/10.1016/j.tws.2014.12.009>.
2. Abramowicz W. Thin-walled structures as impact energy absorbers. *Thin-Walled Structures*, 2003. doi:10.1016/S0263-8231(02)00082-4, [https://doi.org/10.1016/S0263-8231\(02\)00082-4](https://doi.org/10.1016/S0263-8231(02)00082-4).
3. Al-Garni A, Abdelrahman W, Abdallah A. ANN-based failure modeling of classes of aircraft engine components using radial basis functions. *Eksploatacja i Niezawodność* 2019; 21(2): 311–317, <https://doi.org/10.17531/ein.2019.2.16>.
4. Alavi Nia A, Parsapour M. Comparative analysis of energy absorption capacity of simple and multi-cell thin-walled tubes with triangular,

- square, hexagonal and octagonal sections. *Thin-Walled Structures* 2014; 74: 155–165, <https://doi.org/10.1016/j.tws.2013.10.005>.
5. Alexander J M. An approximate analysis of the collapse of thin cylindrical shells under axial loading. *Quarterly Journal of Mechanics and Applied Mathematics* 1960; 13: 10–15.
 6. Alghamdi A A A. Collapsible impact energy absorbers: An overview. *Thin-Walled Structures* 2001. doi:10.1016/S0263-8231(00)00048-3, [https://doi.org/10.1016/S0263-8231\(00\)00048-3](https://doi.org/10.1016/S0263-8231(00)00048-3).
 7. Ali M, Ohioma E, Kraft F, Alam K. Theoretical, numerical, and experimental study of dynamic axial crushing of thin walled pentagon and cross-shape tubes. *Thin-Walled Structures* 2015. doi:10.1016/j.tws.2015.04.007, <https://doi.org/10.1016/j.tws.2015.04.007>.
 8. Badora M, Sepe M, Bielecki M et al. Predicting length of fatigue cracks by means of machine learning algorithms in the small-data regime. *Eksploracja i Niezawodność* 2021; 23(3): 575–585, <https://doi.org/10.17531/EIN.2021.3.19>.
 9. Baroutaji A, Sajjia M, Olabi A G. On the crashworthiness performance of thin-walled energy absorbers: Recent advances and future developments. *Thin-Walled Structures* 2017. doi:10.1016/j.tws.2017.05.018, <https://doi.org/10.1016/j.tws.2017.05.018>.
 10. Baykasoğlu A, Baykasoğlu C, Cetin E. Multi-objective crashworthiness optimization of lattice structure filled thin-walled tubes. *Thin-Walled Structures* 2020. doi:10.1016/j.tws.2020.106630, <https://doi.org/10.1016/j.tws.2020.106630>.
 11. Chen D H, Ozaki S. Circumferential strain concentration in axial crushing of cylindrical and square tubes with corrugated surfaces. *Thin-Walled Structures* 2009; 47(5): 547–554, <https://doi.org/10.1016/j.tws.2008.10.003>.
 12. Chen W, Wierzbicki T. Relative merits of single-cell, multi-cell and foam-filled thin-walled structures in energy absorption. *Thin-Walled Structures* 2001. doi:10.1016/S0263-8231(01)00006-4, [https://doi.org/10.1016/S0263-8231\(01\)00006-4](https://doi.org/10.1016/S0263-8231(01)00006-4).
 13. Fang J, Sun G, Qiu N et al. On design optimization for structural crashworthiness and its state of the art. *Structural and Multidisciplinary Optimization* 2017; 55(3): 1091–1119, <https://doi.org/10.1007/s00158-016-1579-y>.
 14. Ferdynus M, Kotelko M, Kral J. Energy absorption capability numerical analysis of thin-walled prismatic tubes with corner dents under axial impact. *Eksploracja i Niezawodność - Maintenance and Reliability* 2018; 20(2): 252–289, <https://doi.org/10.17531/ein.2018.2.10>.
 15. Ferdynus M, Kotelko M, Urbaniak M. Crashworthiness performance of thin-walled prismatic tubes with corner dents under axial impact - Numerical and experimental study. *Thin-Walled Structures* 2019. doi:10.1016/j.tws.2019.106239, <https://doi.org/10.1016/j.tws.2019.106239>.
 16. Ferdynus M, Rozylo P, Rogala M. Energy absorption capability of thin-walled prismatic aluminum tubes with spherical indentations. *Materials* 2020; 13(19): 1–19, <https://doi.org/10.3390/ma13194304>.
 17. Hanssen A G, Langseth M, Hopperstad O S. Static and dynamic crushing of square aluminum extrusions with aluminum foam filler. *International Journal of Impact Engineering* 2000. doi:10.1016/S0734-743X(99)00169-4, [https://doi.org/10.1016/S0734-743X\(99\)00169-4](https://doi.org/10.1016/S0734-743X(99)00169-4).
 18. Jafarzadeh-aghdam N, Schröder K. Thin-Walled Structures Mechanism of reproducible axial impact of square crash boxes. *Thin-Walled Structures* 2022; 176(February): 109062, <https://doi.org/10.1016/j.tws.2022.109062>.
 19. Jones N. *Structural Impact*. 1990. doi:10.1017/cbo9780511624285, <https://doi.org/10.1017/cbo9780511624285>.
 20. Karagiozova D, Jones N. Dynamic buckling of elastic-plastic square tubes under axial impact - II: Structural response. *International Journal of Impact Engineering* 2004; 30(2): 167–192, [https://doi.org/10.1016/S0734-743X\(03\)00062-9](https://doi.org/10.1016/S0734-743X(03)00062-9).
 21. Kazi M K, Eljack F, Mahdi E. Design of composite rectangular tubes for optimum crashworthiness performance via experimental and ANN techniques. *Composite Structures* 2022; 279(July 2021): 114858, <https://doi.org/10.1016/j.compstruct.2021.114858>.
 22. Kosucki A, Stawiński Ł, Malenta P et al. Energy consumption and energy efficiency improvement of overhead crane's mechanisms. *Eksploracja i Niezawodność* 2020; 22(2): 322–330, <https://doi.org/10.17531/ein.2020.2.15>.
 23. Laban O, Gowid S, Mahdi E, Musharavati F. Experimental investigation and artificial intelligence-based modeling of the residual impact damage effect on the crashworthiness of braided Carbon/Kevlar tubes. *Composite Structures* 2020. doi:10.1016/j.compstruct.2020.112247, <https://doi.org/10.1016/j.compstruct.2020.112247>.
 24. Langseth M, Hopperstad O S, Berstad T. Crashworthiness of aluminum extrusions: Validation of numerical simulation, effect of mass ratio and impact velocity. *International Journal of Impact Engineering* 1999; 22(9): 829–854, [https://doi.org/10.1016/S0734-743X\(98\)00070-0](https://doi.org/10.1016/S0734-743X(98)00070-0).
 25. Lee S, Hahn C, Rhee M, Oh J E. Effect of triggering on the energy absorption capacity of axially compressed aluminum tubes. *Materials and Design* 1999; 20(1): 31–40, [https://doi.org/10.1016/S0261-3069\(98\)00043-0](https://doi.org/10.1016/S0261-3069(98)00043-0).
 26. Liu W, Lin Z, He J et al. Crushing behavior and multi-objective optimization on the crashworthiness of sandwich structure with star-shaped tube in the center. *Thin-Walled Structures* 2016; 108: 205–214, <https://doi.org/10.1016/j.tws.2016.08.021>.
 27. Lu G, Yu T. *Energy Absorption of Structures and Materials*. 2003. doi:10.1533/9781855738584, <https://doi.org/10.1533/9781855738584>.
 28. Luo Y, Fan H. Energy absorbing ability of rectangular self-similar multi-cell sandwich-walled tubular structures. *Thin-Walled Structures* 2018; 124(March 2017): 88–97, <https://doi.org/10.1016/j.tws.2017.11.042>.
 29. Marzbanrad J, Ebrahimi M R. Multi-Objective Optimization of aluminum hollow tubes for vehicle crash energy absorption using a genetic algorithm and neural networks. *Thin-Walled Structures* 2011; 49(12): 1605–1615, <https://doi.org/10.1016/j.tws.2011.08.009>.
 30. Mirzaei M, Shakeri M, Sadighi M, Akbarshahi H. Crashworthiness design for cylindrical tube using neural network and genetic algorithm. *Procedia Engineering* 2011; 14: 3346–3353, <https://doi.org/10.1016/j.proeng.2011.07.423>.
 31. Nia A A, Hamedani J H. Comparative analysis of energy absorption and deformations of thin walled tubes with various section geometries. *Thin-Walled Structures* 2010. doi:10.1016/j.tws.2010.07.003, <https://doi.org/10.1016/j.tws.2010.07.003>.
 32. Paygozar B, Dizaji S A. Investigating Energy Absorption Accessible by Plastic Deformation of a Seismic Damper Using Artificial Neural Network. *Procedia Structural Integrity* 2019; 21(January): 138–145, <https://doi.org/10.1016/j.prostr.2019.12.095>.
 33. Pirmohammad S, Marzdashti S E. Crushing behavior of new designed multi-cell members subjected to axial and oblique quasi-static loads. *Thin-Walled Structures* 2016; 108: 291–304, <https://doi.org/10.1016/j.tws.2016.08.023>.
 34. Rai V, Ghasemnejad H, Watson J W et al. Developed trigger mechanisms to improve crush force efficiency of aluminium tubes. *Engineering Structures* 2019. doi:10.1016/j.engstruct.2019.109620, <https://doi.org/10.1016/j.engstruct.2019.109620>.
 35. Reddy S, Abbasi M, Fard M. Multi-cornered thin-walled sheet metal members for enhanced crashworthiness and occupant protection. *Thin-Walled Structures* 2015. doi:10.1016/j.tws.2015.03.029, <https://doi.org/10.1016/j.tws.2015.03.029>.
 36. Rogala M, Gajewski J, Ferdynus M. Numerical analysis of the thin-walled structure with different trigger locations under axial load. *IOP Conference Series: Materials Science and Engineering* 2019. doi:10.1088/1757-899X/710/1/012028, <https://doi.org/10.1088/1757-899X/710/1/012028>.
 37. Seyedi M R. A Study of Multi-Objective Crashworthiness Optimization of the Thin-Walled Composite Tube under Axial Load. 2020:

- 438–452.
38. Sharifi S, Shakeri M, Fakhari H E, Bodaghi M. Experimental investigation of bitubal circular energy absorbers under quasi-static axial load. *Thin-Walled Structures* 2015. doi:10.1016/j.tws.2014.12.008, <https://doi.org/10.1016/j.tws.2014.12.008>.
 39. Winzer R, Glinicka A. The static and dynamic compressive behaviour of selected aluminium alloys. *Engineering Transactions* 2011; 59(2): 85–100.
 40. Xu F, Zhang X, Zhang H. A review on functionally graded structures and materials for energy absorption. *Engineering Structures* 2018; 171(February): 309–325, <https://doi.org/10.1016/j.engstruct.2018.05.094>.
 41. Yang X, Ma J, Wen D, Yang J. Crashworthy design and energy absorption mechanisms for helicopter structures: A systematic literature review. *Progress in Aerospace Sciences* 2020; 114(June): 100618, <https://doi.org/10.1016/j.paerosci.2020.100618>.
 42. Yin H, Wen G, Liu Z, Qing Q. Crashworthiness optimization design for foam-filled multi-cell thin-walled structures. *Thin-Walled Structures* 2014; 75: 8–17, <https://doi.org/10.1016/j.tws.2013.10.022>.
 43. Yuen S C K, Nurick G N. The energy-absorbing characteristics of tubular structures with geometric and material modifications: An overview. *Applied Mechanics Reviews* 2008; 61(1–6): 0208021–02080215, <https://doi.org/10.1115/1.2885138>.
 44. Zarei H R, Kröger M. Optimization of the foam-filled aluminum tubes for crush box application. *Thin-Walled Structures* 2008; 46(2): 214–221, <https://doi.org/10.1016/j.tws.2007.07.016>.
 45. Zhang X, Cheng G, Wang B, Zhang H. Optimum design for energy absorption of bitubal hexagonal columns with honeycomb core. *International Journal of Crashworthiness* 2008; 13(1): 99–107, <https://doi.org/10.1080/13588260701731732>.
 46. Zhang X, Cheng G, You Z, Zhang H. Energy absorption of axially compressed thin-walled square tubes with patterns. *Thin-Walled Structures* 2007; 45(9): 737–746, <https://doi.org/10.1016/j.tws.2007.06.004>.
 47. Zhang X, Huh H. Energy absorption of longitudinally grooved square tubes under axial compression. *Thin-Walled Structures* 2009. doi:10.1016/j.tws.2009.07.003, <https://doi.org/10.1016/j.tws.2009.07.003>.
 48. Zhang X, Wen Z, Zhang H. Axial crushing and optimal design of square tubes with graded thickness. *Thin-Walled Structures* 2014. doi:10.1016/j.tws.2014.07.004, <https://doi.org/10.1016/j.tws.2014.07.004>.
 49. *Crashworthiness of vehicles*. London, Mechanical Engineering Publications Limited: 1978.
 50. *Structural crashworthiness*. London, Butterworths: 1983.
 51. *Structural impact and crashworthiness*. New York, Elsevier Applied Science Publishers: 1984.